Initiation and early-stage growth of internal fatigue cracking under very-high-cycle fatigue regime at high temperature

Z. Zhao[a*], F. Zhang[b], C. Dong[b], X. Yang[b], B. Chen[c*]

[a]*School of Materials Science and Engineering, Beihang University, Beijing 100191, China*

[b]*School of Energy and Power Engineering, Beihang University, Beijing 100191, China*

[c]*School of Engineering, University of Leicester, Leicester, LE1 7RH, UK*

*Corresponding authors. E-mail address: *bo.chen@leicester.ac.uk, *zhzh@buaa.edu.cn

Abstract

The initiation and early-stage crack growth under very-high-cycle fatigue (VHCF) at room temperature, 750 °C and 850 °C on directionally-solidified Ni-base superalloy have been investigated. There was little frequency effect of 20 kHz on fatigue lives when compared with 100 Hz, nor did the deformation and fracture mechanisms. Dislocation tangles re-arranged themselves to form well-defined networks at interface of γ/γ′, accounting for the enhanced fatigue strength at 850 °C in VHCF regime when compared to that at 750 °C. In most cases, internal casting pore was the crack initiation site. Crack initiation and early-stage growth occurred on one of the {111} planes or their intersecting planes, a characteristic of Stage I cracking. With the use of optimized intermittent loading conditions, both the initiation and early-stage crack growth processes were successfully tracked on the basis of fine but visible beach marks within the Stage I cracking region. The first registered fatigue beach mark can be as close as only 86 μm to the crack initiation site and the crack length increased steadily over the whole early-stage crack growth stage. The enhanced fatigue strength at 850 °C can be rationalized with the higher threshold for propagating the early-stage crack. The fraction of fatigue life consumed for early-stage crack growth reduces with the decreasing stress, eventually leading to the initiation-controlling VHCF fatigue failure. The implications of these results are discussed with respect to the model prediction of fatigue life and fatigue strength.

Keywords: Damage initiation, High-temperature fatigue, Very high cycle fatigue, Microstructure, Ni-base superalloys

1. Introduction

Fatigue is the single largest failure reason based on the jet engine component distress mode statistics.[1] All engine parts should have a minimum fatigue life of 10^9 cycles[2] and this number is based on both the laboratory observations and lessons learned from the industry that a fatigue endurance limit (defined as the lower limiting stress amplitude at $N_f=10^7$) does not exist for most metals.[3] An internal fatigue failure mode is particularly important for fatigue life in the very-high-cycle fatigue (VHCF) regime.[4,5] The most characteristic feature of this failure mode is that the fracture surface exhibits a "fish-eye".[6] In almost all cases the fish-eye appears circular, with a dark area in the center, inside which the crack initiation site is located. Controversy exists as to the presence of this dark area, hence terms of for example optically dark area, fine granular area, granular bright facet,[6] reflect different crack initiation mechanisms and early-stage crack growth behavior that cause such a macroscopic feature.

The origin of internal fatigue cracking can be attributed to the presence of the material discontinuity, including non-metallic inclusions[7–11], casting pores[12,13], second-phase particles[14], and some microstructural inhomogeneities[15,16] for a wide range of alloys (e.g. steel[16–20], titanium[15], aluminum[21] and Ni-base superalloys in a form of single-crystal[14,22], directionally-solidified[23] and polycrystal[9,24,25]). In VHCF regime, the cycles spent for the crack initiation can account for a very large fraction of the fatigue life (i.e. N_i/N_f being greater than 90% and up to 99%[6,7,20,26]). In principle, the fatigue life consumed for crack initiation under VHCF regime should involve both the initiation and early-stage growth process. Unfortunately, their underlying mechanisms have not been fully understood yet.[18,27]

The primary limitation to study VHCF crack initiation and early-stage growth is the lack of experimental method to monitor the internal cracking, although there are many techniques for surface fatigue cracking.[28] As a consequence, attempts to characterize the early-stage growth kinetics of an interior fatigue crack were based on modelling approach that often involves the calculation by subtraction together with the integration of the classic Paris law.[6] For example, Li et al.[5] claimed that the crack propagated at a slow rate of below 10^{-10} m/cycle within the fish-eye. Similarly, the early-stage crack growth rate for Cr-Mo steels under VHCF loading was estimated as 10^{-12} to 10^{-11} m/cycle.[11,29] By the use of variable amplitude loading method to create imprints on the fracture surface, Sun et al.[30] reported that the early-stage crack growth rate was in the magnitude of 10^{-12} to 10^{-11} m/cycle for martensitic stainless steel.

Both the initiation and early-stage crack growth are important to develop a full understanding of VHCF interior failure mode; this forms the motivation of the present work. An experimental method has been developed on the basis of previous VHCF work[31–33] to imprint the fracture surface with regularly spaced beach marks within the early-stage crack growth region on a high-temperature VHCF loaded directionally-solidified Ni-base superalloy. Although such a fracture-surface analysis method is commonly used to trace back the crack growth history (e.g. Reference[34]), no work has been done to measure the crack growth kinetics in high-temperature VHCF regime, particularly for the crystallographic Stage I cracking, a predominant process for early-stage crack growth in Ni-base superalloys. This cracking mode is distinct from the subsequent Stage II cracking, which occurs in a direction perpendicular to the principal stress axis.[35]

A fractographic study of Stage I fatigue cracking on MAR-M200 Ni-base superalloy was performed by Duguette et al.[36] Observations of featureless or rubbed Stage I fracture surfaces suggested that crack propagation was a continuation of crack initiation, instead of a discrete process. By using compact-tension samples with the notch and pre-crack, Stage I crack propagation rates along crystallographic planes were measured to be between 8.11×10^{-9} and 2.09×10^{-7} m/cycle on single-crystal NKH-304, depending on the specific loading direction with respect to the crystallographic orientation.[37] The lowest crack propagation rate was measured to be 1×10^{-8} m/cycle on single-crystal CMSX-2.[38] Since the stress intensity factor close to the crack initiation site in pre-cracked sample is different to that of a natural crack initiated on unnotched sample, such a high crack growth rate is probably not representative of the VHCF crack initiation and its early-stage growth. Note the calculated early-stage crack growth rate as reported in References[11,29,30] for steels under VHCF regime were in the range of 10^{-12} to 10^{-11} m/cycle; they differed apparently by a factor of about 10^3.

In the present work, the fatigue crack initiation and early-stage crack growth in a directionally-solidified Ni-base superalloy was examined in VHCF and high-cycle fatigue regime at both room and elevated temperatures using ultrasonic fatigue machine operating at 20 kHz. Comparative fatigue tests were performed at 100 Hz to clarify the frequency effect. Quantitative fractography analysis was performed to characterize the early-stage crack growth behavior in addition to identify the preceding crack initiation mechanism and the subsequent crack deflection. The deformation mechanism as a function of temperatures was also elucidated by using transmission electron microscopy (TEM). Finally, both the fatigue strength and lifetime predictions were made and compared against experimental data.

2. Material and Experimental

2.1 Material

DZ125 is a γ' precipitation-strengthened directionally-solidified alloy that is characteristic of high Al and Ti contents and Hf-rich. This alloy, similar to Rene 142 and CM247LC in terms of Al, Ti and Hf contents, is a columnar-grained turbine blade superalloy and the maximum service temperature is 1050 °C. The material was supplied in a bar shape with each dimension of 15 mm in diameter and 165 mm in length. The chemical composition of as-supplied DZ125 alloy was confirmed using inductively coupled plasma atomic emission spectroscopy and the result is presented in Table 1.

Table 1. Chemical composition of as-supplied DZ125 alloy (in wt%)

C	Cr	Co	Mo	W	Ta	Ti	Al	B	Hf	Si	Ni
0.11	8.96	10.04	2.05	7.10	3.83	1.02	5.18	0.016	1.59	<0.10	Bal.

The material had been subjected to the heat treatment cycle by first solution annealing at 1180 °C for 2 h and then 1230 °C for 3 h; second two-step aging at 1100 °C for 4 h and then 870 °C for 20 h. Table 2 provides tensile properties of this alloy at both room (RT) and elevated temperatures (750 and 850 °C). These properties were obtained by using MTS 810 test system on round bar specimen (5 mm in diameter and 35 mm in gauge length) at constant displacement rate of 1 mm/min. As expected, the tensile strength decreased but ductility increased with increasing temperature. Micro-hardness measurements at RT were performed on an FM-7000A instrument and 10 individual points were collected to derive the average value.

Micro-hardness at 750 °C and 850 °C were derived from the measured tensile strength using the conversion factors as reported in GB T1172-1999.

The microstructure consists of 60.0% γ′-volume fraction; a representative SEM micrograph is shown in Fig. 1a and the average γ′-size was measured to be 0.45±0.09 μm. More details about DZ125 alloy can be found in our previous work.[39] Fig. 1b shows the overall columnar grain structure and the grain width and dendrite width were measured as 883.3±40.5 μm and 202.5±23.6 μm respectively.

Table 2 Tensile properties of DZ125 alloy in the fully heat treated condition.

Temperature (°C)	$\sigma_{0.2}$ (MPa)	Tensile strength (MPa)	Elongation (%)	Vickers hardness
23	968	1223	16.1	400
750	887	1177	21.5	386
850	775	991	28.4	330

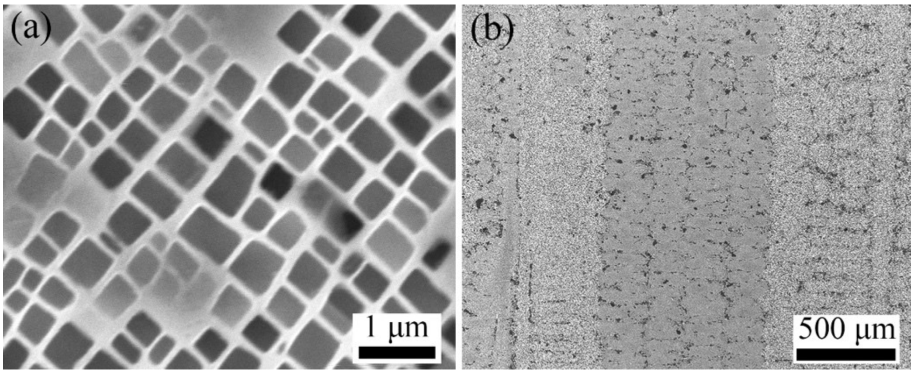

Fig. 1: (a) γ’ precipitate microstructure after solution annealing and two-step aging; (b) an optical micrograph showing the columnar grain structure and dendrites

2.2 Fatigue testing

Shimadzu USF-2000 ultrasonic fatigue testing system was used to perform the VHCF tests at 20 kHz and the specimen was loaded in tension-compression (stress ratio R=-1), Fig. 2a. Specimens were all machined out from the superalloy bars along their longitudinal direction and the loading direction was parallel to the <001> crystallographic orientation. The alternating stress σ_a levels ranged from 250 MPa to 500 MPa to establish the stress-life S-N curves for RT, 750 °C and 850 °C.

A self-designed cooling gas nozzle was used to compensate the specimen self-heating due to very-high frequency at RT, while reduce the temperature of the loading bar at high temperature VHCF tests, Fig. 2b. A FOTRIC 220 infrared thermal camera was set up to examine the temperature change, Fig. 2a. Stress levels were incrementally increased from σ_a=225 MPa to 325 MPa with step size of 25 MPa. It was confirmed that the temperature rise for the RT tests was less than 15 °C; hence the effect of specimen self-heating is limited. In terms of high-temperature VHCF tests, the specimen was heated by using induction coils integrated with a closed-loop temperature controller, as illustrated in Fig. 2a. The surface-temperature was kept within ±5 °C of the test temperature.

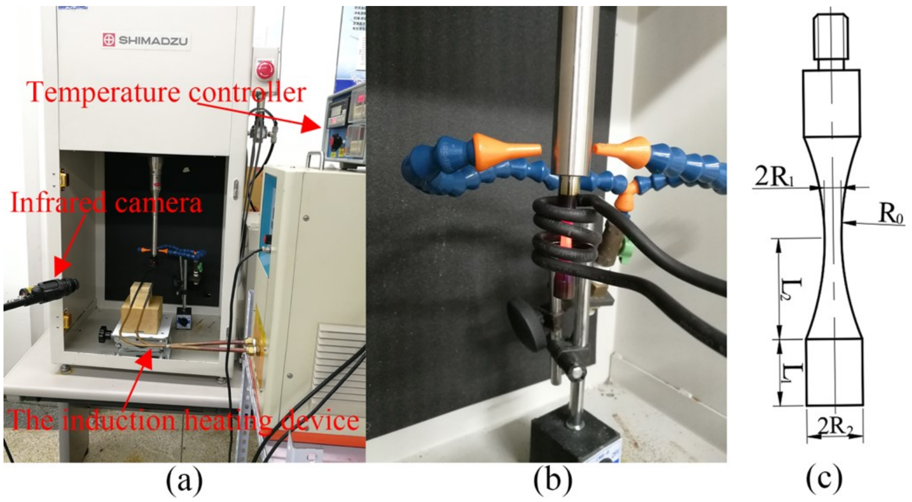

Fig. 2: (a) High-temperature ultrasonic VHCF fatigue testing system; (b) A closer view of the high-temperature test assembly; (c) VHCF fatigue specimen design

The dimension of the specimen is axisymmetric with a reduced section at the center and a circular profile, Fig. 2c. Analytical solution is available for specimen design with a hyperbolic cosine profile and the difference between this idealized profile and the circular profile (Fig. 2c) is small, as described in Reference[40], hence the resonance length and the stress distribution of the ultrasonic fatigue specimen were derived based on the analytical solution, to avoid unnecessary numerical calculation. The temperature gradient over 5 mm distance to the minimum sectional area was less than 5 °C. Therefore, the effect of temperature gradient on the VHCF specimen design is insignificant.

In brief, the one-dimensional longitudinal wave equation for an axisymmetric specimen with a varying cross section can be described as:

$$\rho S(x)\frac{\partial^2 u(x,t)}{\partial t^2} - E_d\left[S'(x)\frac{\partial u(x,t)}{\partial x} + S(x)\frac{\partial^2 u(x,t)}{\partial x^2}\right] = 0 \quad (1)$$

where ρ is material's density, $S(x)$ is the area section at position x and $u(x,t)$ is the displacement function of the specimen at position x and time t. E_d is the material's dynamic elastic modulus (temperature-dependent) which determines the vibration generated stress magnitude through the relation:

$$F(x,t)=E_{\mathrm{d}}S(x)\frac{\partial u(x,t)}{\partial x} \tag{2}$$

By separating the displacement function as $u(x,t)=U(x)\sin\omega t$, applying the boundary conditions and the hyperbolic cosine profile function (Eq. 3), the analytical solution of resonance length L_1 is given in Eq. 4.

$$\begin{cases} y(x)=R_2 & L_2<|x|<L_2+L_1 \\ y(x)=R_1\cosh(\alpha x) & |x|<L_2 \end{cases} \tag{3}$$

$$L_1=\frac{1}{k}\arctan\left\{\frac{1}{k}\left[\frac{\beta}{\tanh(\beta L_2)}-\alpha\tanh(\alpha L_2)\right]\right\} \tag{4}$$

where $\alpha=\frac{1}{L_2}\operatorname{arccos}h(\frac{R_2}{R_1})$, β takes the form as given in Eq. 5. The maximum stress at the position corresponding to the minimum sectional area in the hourglass type specimen (Fig. 2c), i.e. the testing stress $\sigma_{\max}$, is eventually obtained as:

$$\sigma_{\max}=E_{\mathrm{d}}\frac{\partial U(x)}{\partial x}\Big|_{x=0}=\beta E_{\mathrm{d}}A_0\varphi(L_1,L_2)$$

$$\text{where }\begin{cases} \beta=\sqrt{\alpha^2-k^2} \\ \varphi(L_1,L_2)=\dfrac{\cos(kL_1)\cosh(\alpha L_2)}{\sinh(\beta L_2)} \end{cases} \tag{5}$$

In practice, we defined specimen dimensions of R_1, R_2, L_2 by considering the testing condition, material availability as well as difficulties to achieve the desired surface finish, then L_1 was calculated based on Eq. 4. Table 3 provides the VHCF specimen dimensions for RT, 750 °C and 850 °C, respectively. The dynamic elastic modulus E_d was measured by using the resonant frequency in longitudinal mode of vibration. For the RT VHCF tests, the radius of the specimen, R_1=1.5 mm and R_2=5.0 mm, and the length at varying cross section region, L_2=15 mm, were used. As a result, the resonance length L_1 was calculated as 8.46 mm by knowing E_d=127 GPa and ρ=8.595 g/cm^3, Table 3. Using the same approach but with different values of dynamic elastic moduli, i.e. E_d=103 GPa for 750 °C and E_d=96 GPa for 850 °C (Table 3), the high-temperature VHCF specimen was designed with the same dimension of R_1=2.5 mm, R_2=5.0 mm, L_2=20 mm, but the length L_1 of being 8.50 mm for 750 °C and 7.63 mm for 850 °C, respectively.

Table 3 Parameters used for the VHCF fatigue specimen design

Temperature (°C)	Dynamic elastic modulus, E_d (GPa)	ρ (g/cm^3)	R_1 (mm)	R_2 (mm)	L_2 (mm)	L_1 (mm)
23	127		1.5		15	8.46
750	103	8.595	2.5	5.0	20	8.50
850	96		2.5		20	7.63

Both the continuous and intermittent excitations were used for the VHCF ultrasonic fatigue testing. A pre-defined pulsed excitation was used to create many regularly spaced fatigue beach marks within the early-stage crack growth region. Table 4 provides the pulse/pause conditions for the VHCF loading at elevated temperatures. The formation mechanism of fatigue beach marks on fracture surface have been thoroughly discussed in for example References[41,42]. There are several studies[30–33,43–45] carried out in the VHCF field with some interesting comments about the creation of beach marks and we will discuss them in detail in Section 4.4. For the VHCF loading at RT, we did not record the detailed pulse/pause conditions, but less than 4 beach marks was found based on the SEM fractography examination.

Table 4 Summary of intermittent fatigue loading with pre-defined pulse/pause conditions.

Temperature (°C)	Alternating stress (MPa)	Cycles to failure N_f	Pulse/pause conditions (ms)	Distance of the first registered beach mark to crack initiation site
750	300	5.20×10^5	500/500	86 μm
750	275	3.36×10^7	200/200	127 μm
850	350	1.04×10^6	120/840	700 μm
850	300	6.87×10^7	120/720	533 μm

The fatigue life obtained by ultrasonic fatigue testing system at both RT and 750 °C was compared to similar data generated on QBG-100 high-frequency fatigue tester that operated at 100 Hz to assess the frequency effect. Standard round-bar fatigue specimens were used in accordance with the Aviation Industry Standard of China HB 5287-96[46]. A three-zone split furnace was used to heat the specimen to targeting temperature of 750 °C with fluctuation of ±5 °C.

2.3 Microstructural characterization

Metallographic samples were first ground with 60 to 3000 grit SiC papers, and then polished down to 1 μm diamond suspension. Chemical etching was performed using 5 g $CuSO_4$ + 15 ml HCl + 25 ml H_2O to reveal the general microstructure. To reveal γ′-precipitate morphology, electrolytic etching was used with a solution of 70 ml H_3PO_4 and 30 ml H_2O at 5 V for 4 s.

Fractography examination to study crack initiation and growth was carried out on post-fatigued specimens using Zeiss Supra 55-VP FEGSEM under either secondary electron (SE) or backscattered electron (BSE) imaging mode. Local regions of crack initiation were carefully examined to identify the origin of fatigue cracking and to measure characteristic dimensions of the crack initiation site. The early-stage crack growth rate was measured quantitatively based on the fatigue beach marks that had been created by using the pulse/pause conditions in Table 4. Metallographic samples were also extracted from the location of 5 mm below the fractured surface to study the morphological change of γ′-precipitates.

Tecnai G^2 20 TEM operating at 200 kV was used to characterize the dislocation interaction with γ′-precipitates. TEM samples were extracted close to the fatigue crack initiation site, i.e. within 0.5 mm distance to the fractured surface. Although the direct TEM observation of crack-tip deformation behavior was not carried out, the plastic zone at the crack tip should be limited as the applied stress is much lower than the macro-scopic yield strength. Therefore, the present TEM observation is very likely to reveal the deformation mechanism related to the fatigue crack initiation.

3. Results

3.1 Fatigue strength

The S-N data curve generated by ultrasonic fatigue testing system are presented in Fig. 3 and totally 36 individual tests were performed. These data cover the fatigue life regime of N_f=3×10^5 to 4×10^8. The fatigue test run-out was considered when exceeding 10^9 cycles, but with the exception of one 850 °C test (i.e. interrupted after 10^8 cycles). Fatigue strength is used here to specify the alternating stress σ_a value (or the average value) at 10^9 cycles from the S-N curve. Based on this method, the fatigue strength was determined as 262.5 MPa, 250 MPa and 300 MPa for RT, 750 °C and 850 °C, as indicated by the plateaus in Fig. 3.

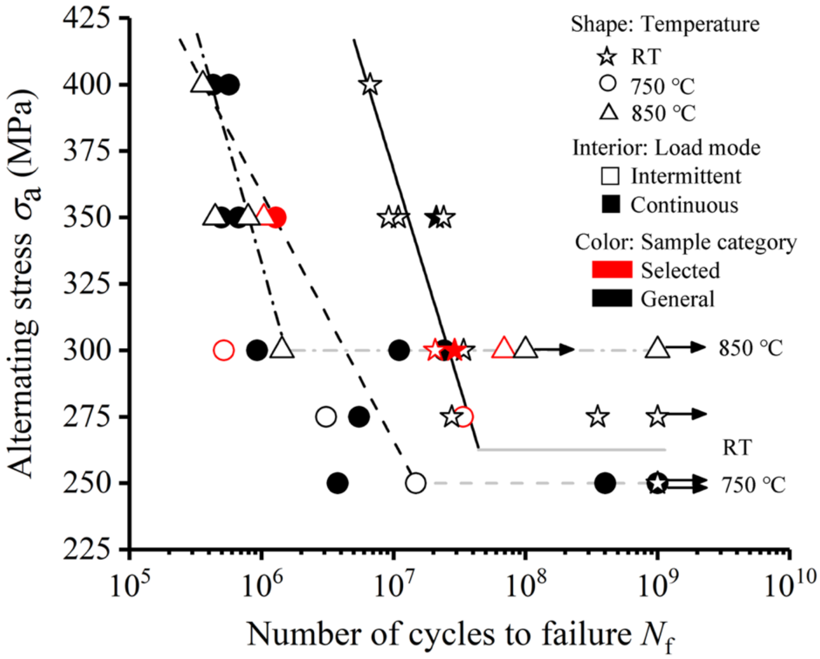

Fig. 3: S-N fatigue diagram generated at 20 kHz at three temperatures of room-temperature (RT), 750 °C and 850 °C. Data with hollow symbols represent those generated with intermittent loading mode, whereas solid symbols represent those generated with continuous loading. Note: the grey color lines were drawn to indicate the best estimated fatigue strength at 10^9 cycles.

It is admitted that the above-mentioned approach might not be the most satisfactory one to determine the VHCF fatigue strength. However, it was not possible to use the staircase test method due to the limited availability of material. To this end, the fatigue strength at 10^9 cycles is used here, instead of fatigue limit. Compared to the previous high-temperature VHCF work[22,23] on Ni-base superalloys, the present work already reported a much higher number of tests particularly in the VHCF regime of N_f=10^7 to 10^9 cycles. Many replicate tests were conducted at the same stress levels to take into account the fatigue intrinsic data scatter.

As shown in Fig. 3, at high stress regime, the RT fatigue strength is much higher than that at 750 °C and 850 °C and the difference between the latter two is marginal. This is probably related to the reduced strengthening effect of γ′-precipitates. The cutting of γ′-precipitates is more likely to occur under the higher stress; hence the overall strength of the material is determined by the γ-matrix that is known to exhibit a monotonic temperature dependence (i.e. strength decreases with increasing temperature). However, at low stress regime (i.e. in the VHCF regime of Fig. 3), the strengthening effect of γ′-precipitates is more dominant. The fatigue strength at 750 °C is slightly lower than that at RT. By comparison, the fatigue strength at 850 °C is higher than that at RT and 750 °C. The enhanced fatigue strength at 850 °C will be discussed in detail in Section 4.3 together with the TEM results. The fatigue life of Inconel 718 at elevated temperatures was also reported to be higher than that obtained at RT.[47] Therefore, the temperature dependence of fatigue strength in the present material is not completely unexpected.

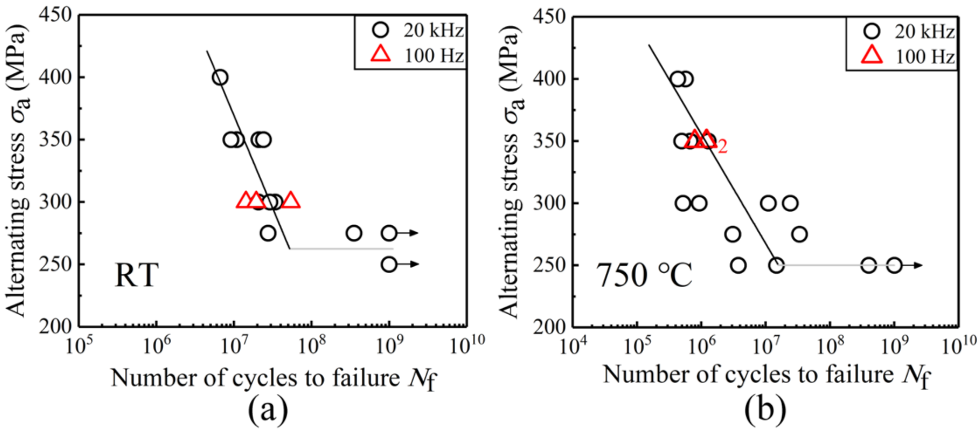

Fig. 4: A comparison of fatigue data generated at 20 kHz with those at 100 Hz showing little frequency effect on DZ125 alloy: (a) RT; (b) 750 °C. Note: the subscript 2 in (b) indicates two overlapping 100 Hz data points.

To assess whether the very-high frequency of 20 kHz employed in ultrasonic fatigue testing would affect the overall fatigue life, six comparative fatigue tests were performed using conventional fatigue tester at a frequency close to 100 Hz. Fig. 4a and 4b compare the 100 Hz fatigue data with those generated at 20 kHz, at two stress levels of σ_a=300 MPa at RT and 350 MPa at 750 °C. All data appear to overlap with each other, indicating little frequency effect at both RT and 750 °C. When fatigue data generated by ultrasonic fatigue and conventional testers on single-crystal PW1484 superalloy were compared, frequency effect was also found to be limited.[14]

3.2 Fatigue crack initiation

All of the fractured specimens were examined under SEM and it was confirmed that fatigue cracks initiated exclusively from the interior. 13 tests were performed at RT and 5 out of 11 failed specimens exhibited crack initiation from the casting pore. 15 tests were performed at 750 °C with 9 out of 14 failed specimens exhibiting crack initiation from the casting pore. By comparison, 8 specimens were tested at 850 °C and 4 out of 6 failed specimens showed crack initiation from the casting pore. Therefore, casting pores are the origin for these interior fatigue cracking in most cases (18 out of 31 fatigue failed specimens).

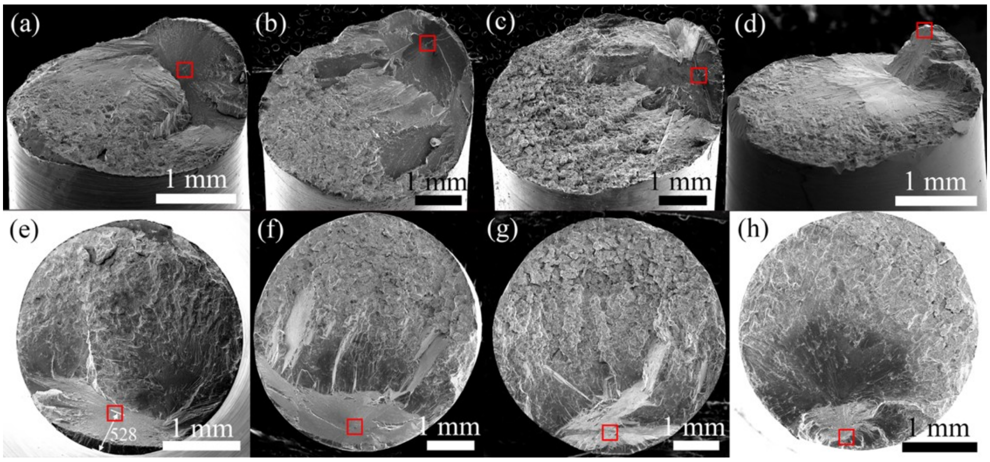

Fig. 5: Overall facture surface of post-fatigue specimens showing the transition from crystallographic Stage I to non-crystallographic Stage II cracking: (a) σ_a=300 MPa, N_f=2.07×10^7, RT; (b) σ_a=275 MPa, N_f=3.40×10^7, 750 °C; (c) σ_a=300 MPa, N_f=6.87×10^7, 850 °C; (d) σ_a=350 MPa, N_f=2.40×10^7, RT; (e) to (h) showing the top view of the fracture surface for the corresponding (a) to (d). Note: the red color box indicates the crack initiation sites with (a) to (c) due to the casting pore, whereas (d) due to the solidification-shrinkage defect.

The characteristics of the fracture surface are described based on the representative SEM micrographs from RT, 750 °C and 850 °C, respectively, and these specimens are indicated by red color symbols in Fig. 3. The overall appearance of VHCF fracture surfaces are shown in Fig. 5a to 5c for the side view, and in Fig. 5e to 5g for the top view. The red color boxes on each figure highlight the crack initiation sites associated with the casting pore. The initial part of the crack is of a shear type, inclined close to the maximum shear stress direction, and the crack appears to grow on a distinctly large crystallographic facet. The average angle of the initial fracture surface was measured as ~52° with respect to the far-field loading axis. As the theoretical angle between the (111) plane-normal and (001) plane-normal is 54.74°, the observed crack initiation and early-stage crack growth is typical of that found in Stage I crystallographic cracking. This is consistent with previous VHCF work on Ni-base superalloys (directionally-solidified[23] and single-crystal[14,22,23,48]). When the Stage I cracks grew and coalesced to a size large enough to propagate under the applied Mode I stress, Stage II crack propagation took place at later stage, Fig. 5. Finally, a rough surface feature can be found at the final failure zone, Fig. 5, which is similar to that often observed on tensile fracture surface.

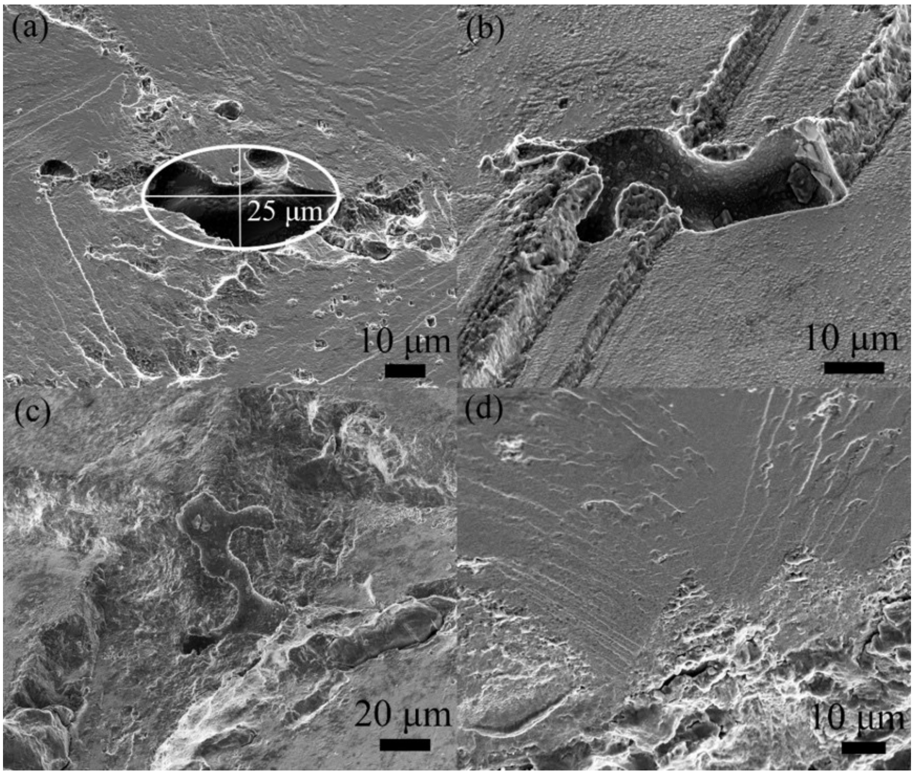

Fig 6: Crack initiation sites for high-temperature VHCF post-fatigue specimens: (a) σ_a=300 MPa and RT, N_f=2.07×10^7; (b) σ_a=275 MPa and 750 °C, N_f=3.40×10^7; (c) σ_a=300 MPa and 850 °C, N_f=6.87×10^7; (d) σ_a=350 MPa, N_f=2.40×10^7, RT. The crack initiation from the casting pores are shown in (a) to (c), whereas that from the solidification-shrinkage defect is shown in (d).

The magnified SEM views of the crack initiation from the casting pore are shown in Fig. 6a, 6b and 6c for RT, 750 °C and 850 °C, respectively. The early-stage crack growth occurred on one or more intersecting {111} crystallographic planes. Fig. 6a illustrates a typical example where the initiation and early-stage crack growth occurred on one of the {111} planes, whereas Fig. 6b represents that occurring on intersecting {111} planes. Notwithstanding that these VHCF tests were performed at different temperatures, all SEM micrographs revealed a single casting pore as the crack initiation site. Furthermore, the microstructural configurations in the vicinity of the casting pores (i.e. the rough surface), Fig. 6a, 6b and 6c, seems to indicate that the cumulative early strain localization would be required to trigger the VHCF crack initiation.

It is important to determine whether these failed specimens fall into the category of near-to-surface or internal pores, hence the method based on the ratio of pore size and its distance to the surface, initially proposed by Murakami [49,50], was adopted. If the ratio is less than a value of 1.6, the pore should be judged as internal pore, otherwise a near-to-surface pore. One measurement example on the fracture surface is shown in Fig. 5e and Fig. 6a. The pore size, defined by the half-length along major axis, was determined as 25 μm, Fig. 6a, and its site distance was 528 μm, Fig. 5e. The calculated ratio of the pore size and its distance to surface ranged from 0.05 and 0.35 for all of the casting pores. Therefore, they should be classified as internal pores. In sum, when internal casting pores are present, fatigue cracks always initiated from this type of material discontinuity in the lifetime of 3×10^5 to 4×10^8 cycles to failure.

For the rest of fractured specimens (13 out of 31), it is not certain what causes the crack initiation although there was some hint pointing towards the solidification-shrinkage defect. A typical example of this type of fracture surface is shown in Fig. 5d and 5h and no measurable casting pore could be identified at the crack initiation site, Fig. 6d. Since the crack initiation mechanism for these specimens is not conclusive, we will not discuss them further. But it is worthwhile to mention that a severe surface roughness at the crack initiation site can be seen in Fig. 6d, and such a localized deformation seems to be similar to that as observed in Fig. 6a to 6c. Putting the S-N data and the type of crack initiation under scrutiny, no correlation could be identified regarding the effect of temperature, stress, or fatigue life on the nature of crack initiation.

3.3 Fatigue crack propagation

Fig. 7a shows a typical imprinted fracture surface within crystallographic Stage I cracking region. Regularly spaced beach marks were created by the 850 °C intermittent VHCF loading with pulses of 120 ms separated by pauses of 840 ms (Table 4). To make it clear how the measurement of early-stage crack growth rate was performed, all the beach marks within the field-of-view of Fig. 7a are indicated by white lines. By knowing the pulse time of 120 ms at 20 kHz, the number of cycles can be derived as 2400. Since the distance between the two adjacent beach marks was measured as 38.43 μm based on the SEM fractography, Fig. 7a, the crack growth rate can then be calculated as 1.60×10^{-8} m/cycle. For comparison purpose, Fig. 7b shows a typical Stage II cracking region. Fatigue striations induced by four fatigue cycles are highlighted in Fig. 7b. The crack growth rate in this later propagation stage was determined as 1.45×10^{-7} m/cycle. Therefore, the crack growth rate within the crystallographic Stage I cracking region was about one order of magnitude lower than that at the later stage that occurred on a non-crystallographic plane. Furthermore, the early-stage fatigue crack growth plane appears to be much smoother, Fig. 7a, indicating a very localized slip activity.

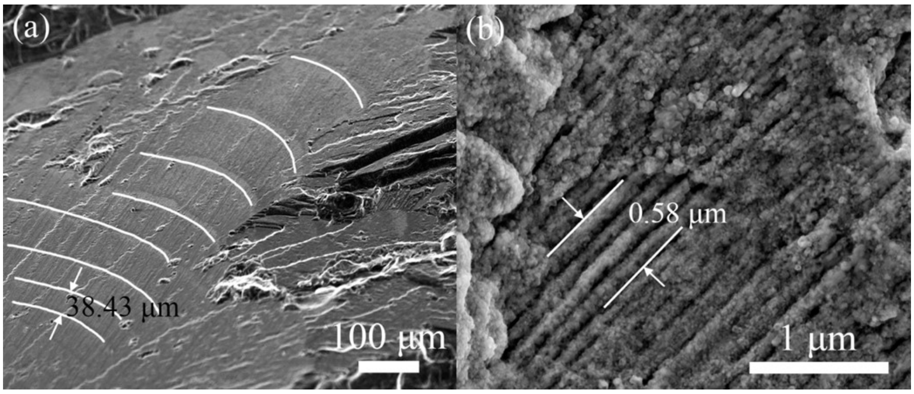

Fig. 7: SEM fractography of the specimen tested at σ_a=350 MPa and 850°C, N_f=1.04×10^6: (a) beach marks revealed in Stage I cracking region; (b) fatigue striations revealed in Stage II cracking region. A pulse/pause time of 120 ms/840 ms was employed.

Fig. 8 presents another example where the fracture surface imprint technique was applied to study the early-stage crack growth behavior at 750 °C. The crack initiated from the casting pore as outlined in Fig. 8a, and the magnified views of Stage I cracking region are shown in Fig. 8b to 8d. By the use of a pulse/pause time of 200 ms/200 ms (Table 4), the regularly spaced beach marks were created on the flat crack propagation plane with two different propagation directions, Fig. 8c and 8d.

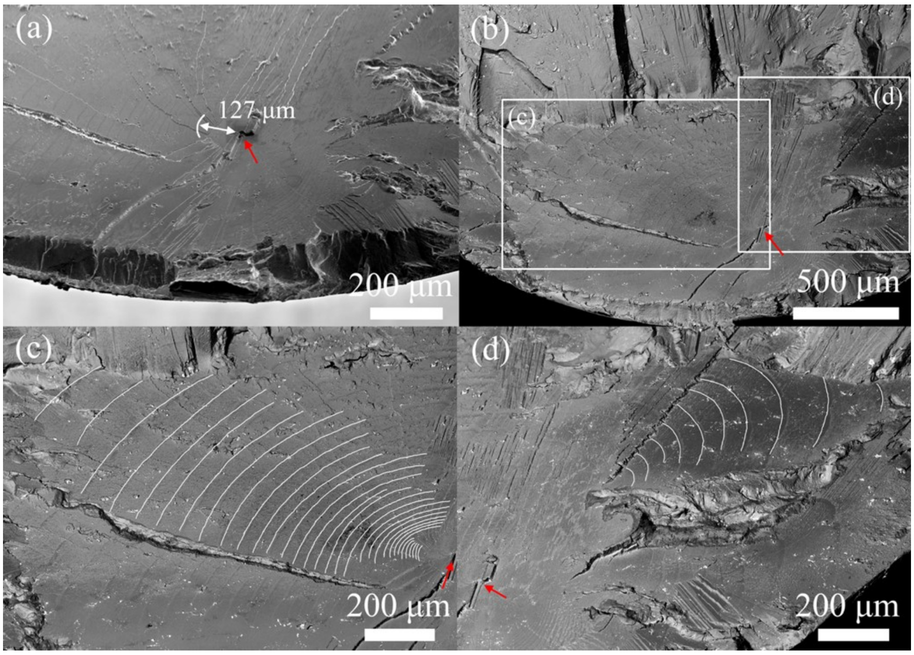

Fig. 8: SEM micrographs showing the imprinted fracture surface with regularly spaced fatigue beach marks within the early-stage crack growth region: (a) SE and (b) BSE images; (c) and (d) are the enlarged views of specified areas in (b). Post-fatigued specimen at σ_a=275 MPa and 750°C, N_f=3.36×10^7. Note: Intermittent loading mode with pulse time/pause time of 200 ms/200 ms was employed.

Quantitative measurements of the cycle-by-cycle crack growth rate, da/dN, were performed on the basis of regularly spaced beach marks within the Stage I cracking region for both 750 °C and 850 °C tests. The measured characteristic crack growth rates (i.e. minimum, mean and maximum) for all four specimens are summarized in Table 5. By assuming that the initial measurable crack length is the distance between the first registered beach mark and the crack initiation site, the stress intensity factor amplitude ΔK can be calculated by considering the crack length increment[51]:

$$\Delta K = \frac{2}{\pi} \sigma_{\mathrm{a}} \sqrt{\pi a} \tag{6}$$

where a is the crack length with the increment corresponding to the distance between two adjacent beach marks. The tension has a predominant effect on the crack growth behavior when the macroscopic plastic deformation is limited.[5] As a result, the alternating stress σ_a level, instead of the stress range, is used for the case of R=-1. The white lines in Fig. 8a indicates the determination of the initial crack length of being 127 μm for the test performed at 750 °C and 275 MPa. For all the other three specimens, their first beach mark distance to the crack initiation site (i.e. initial crack length) are summarized in Table 4.

Table 5. Summary of early-stage crack growth characteristics as determined from the beach marks created by using pre-defined pulse/pause conditions as given in Table 4

Temperature (°C)	σ_a (MPa)	Crack growth rate (10^{-9} m/cycle)			m	The portion of life spent for early-stage crack growth
		Min.	Mean	Max.		
750	300	1.95	11.8	43.8	2.40	44.2%
750	275	1.61	8.9	29.2	2.51	0.38%
850	350	6.10	11.3	23.9	7.87	3.69%
850	300	6.78	15.6	24.8	7.59	0.03%

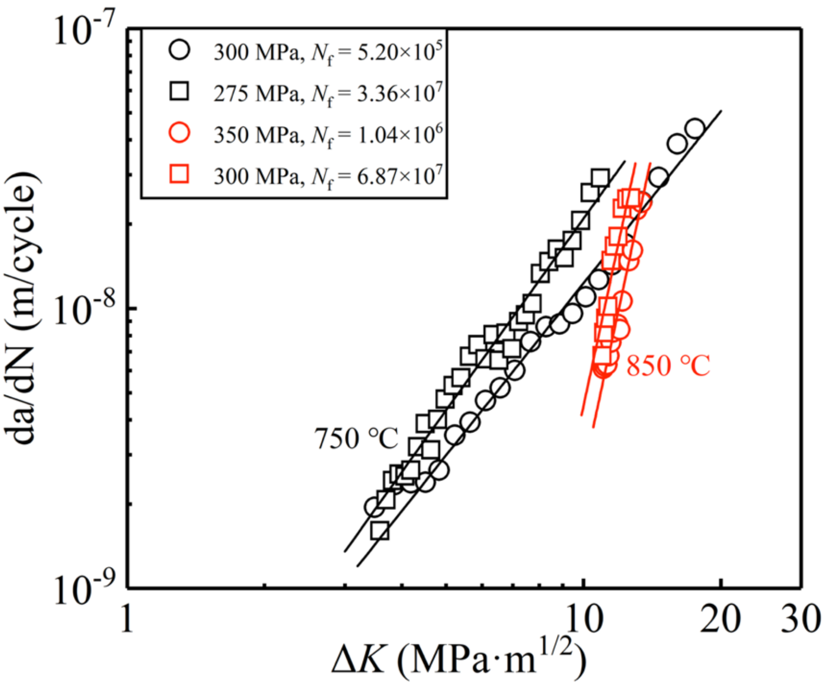

Fig. 9: Early-stage crack growth rate of da/dN versus ΔK (the black symbol represents two 750 °C tests performed at 300 MPa and 275 MPa, while the red symbol represents two 850 °C tests performed at 350 MPa and 300 MPa)

When plotting the measured da/dN versus the calculated ΔK for all four specimens, Fig. 9, it is evident that the early-stage crack growth is governed by the classic Paris law. The Paris law exponent m was determined from all four tests and they are summarized in Table 5. For 750 °C tests, m=2.40 and 2.51 were found for 300 and 275 MPa, respectively, whereas the much higher m value was found for 850

°C tests with m=7.87 and 7.59 for 350 and 300 MPa. Steuer et al. [12] studied the relationship of da/dN and ΔK on single-crystal AM1 at 650 °C under low-cycle fatigue loading and the Paris law exponent m=3.3 was obtained from Reference[52] when describing the crack growth rate. Hence, the m values obtained in 750 °C fatigue are consistent with the previous work. It is important to note that the quantitative measurement of early-stage crack growth rate based on fatigue beach marks created by intermittent loading has not been exploited for the VHCF interior cracking.

3.4 Fatigue deformation mechanisms

Fig. 10a to 10c show the size and morphology of γ′-precipitates in post-fatigued specimens tested under VHCF regime at temperatures of RT, 750 °C and 850 °C respectively. Compared to those that have the average γ′-size of 0.45±0.09 μm at prior to fatigue condition, Fig. 1a, the cuboidal shaped γ′-precipitates had little change as the γ′-size was measured as 0.48±0.13 μm for RT in Fig. 10a, 0.48±0.14 μm for 750 °C in Fig. 10b, and 0.46±0.09 μm for 850 °C in Fig. 10c. Unlike the work by Kraft et al.[53] on thermomechanical fatigue of a single-crystal Ni-base superalloy at high temperatures, no coarsening of the primary γ′-precipitates can be found in the present DZ125 superalloy due to VHCF loading at high temperatures. In addition, the occurrence of rafting is not expected as the tests were performed under fully reversed conditions. The formation of secondary γ′-precipitates within the γ-matrix can be seen for 750 and 850 °C VHCF tests, but their volume fraction was very small.

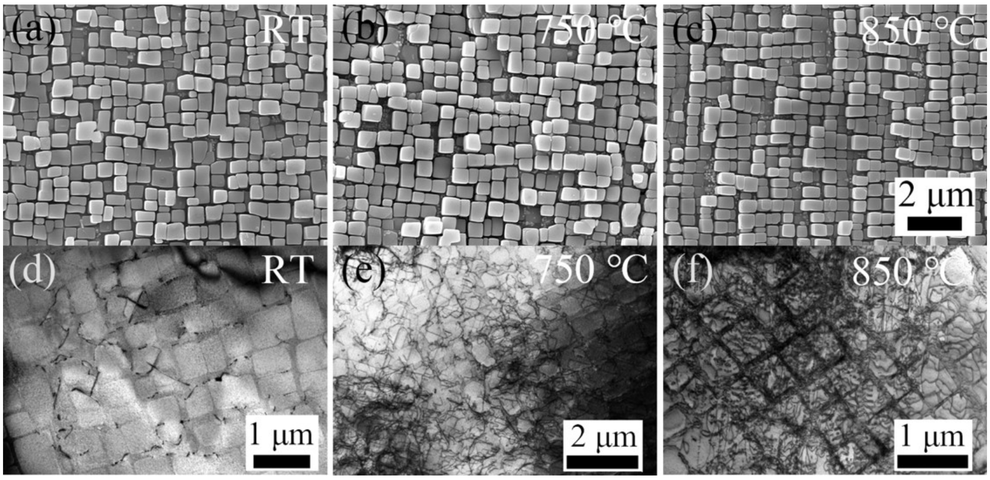

Fig. 10: (a) to (c) SEM micrographs of γ′-precipitates morphology at post-fatigued specimens tested at RT, 750 °C and 850 °C respectively; (d) to (f) corresponding TEM bright-field images showing the dislocation structure and distribution with respect to γ′-precipitates. Specimens were tested at σ_a=300 MPa and RT, N_f=2.92×10^7 for (a) and (d); σ_a=350 MPa and 750 °C, N_f=1.28×10^6 for (b) and (e); σ_a=350 MPa and 850 °C, N_f=1.04×10^6 for (d) and (f)

Fig. 10d shows the dislocation structure and distribution under the VHCF regime at RT. The dislocation density inside the γ′-precipitates is very low, indicating the difficulty for dislocations to penetrate the hard γ′-precipitates under VHCF loading at RT. The inhomogeneous distributed dislocations within γ-channels seems to suggest that the activation of primary slip occurred preferably with high Schmid factor. In addition, no evidence of γ′ shearing was revealed. It is worthwhile to mention that Stocker et al.[54] studied the polycrystalline Ni-base superalloys (e.g. Nimonic 80A) and pure nickel in the VHCF regime at RT. Planar dislocation arrangements were revealed in single grains with favorable grain orientations. The interaction of dislocations with γ′-precipitates was also found to be restricted. Therefore, the dislocation interaction with γ′-precipitates in the VHCF regime does not necessarily involve shearing-type processes that cuts through the γ′-precipitates.

At 750 °C, the presence of dislocation tangles that are spread throughout the γ-channels can be seen in Fig. 10e. More detailed TEM observation, Fig. 11a, revealed that dislocations started to form loops surrounding γ′-precipitates and bowing-out at 750 °C, i.e. the activation of Orowan dislocation-to-particle interaction mechanism[55]. By comparison with the dislocation observation in Fig. 10d for the RT VHCF, it is evident that the dislocation density increased rapidly with the increasing temperature. Again, no evidence of γ′ shearing at 750 °C was found.

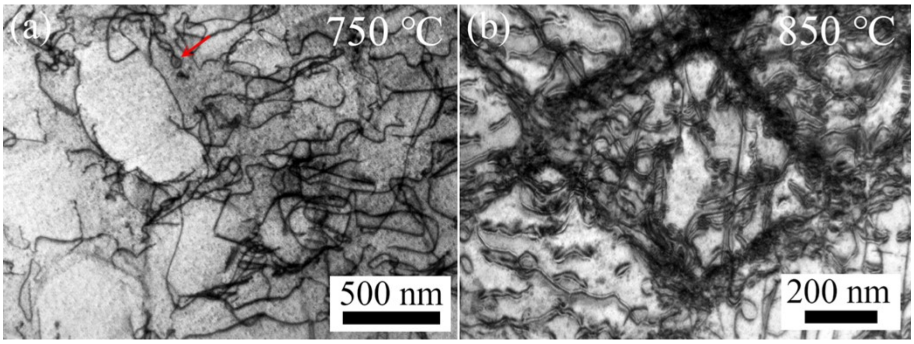

Fig. 11: TEM micrographs of the VHCF fatigued specimen showing typical dislocation structures: (a) specimen tested at σ_a=350 MPa and 750 °C, N_f=1.28×10^6, showing dislocation loops and (b) specimen tested at σ_a=350 MPa and 850 °C, N_f=1.04×10^6 showing well-developed dislocation networks.

With the further temperature increase to 850 °C, tangles of dislocations re-arranged themselves to form interfacial dislocation networks around γ′-precipitates and within the γ-channels (i.e. the interface of γ/γ′), Fig. 10f. The development of well-defined dislocation networks, as revealed clearly in Fig. 11b, indicate the influence of dynamic recovery processes and associated high-temperature dislocation climb and cross-slip at 850 °C.[53,56] Refer to the higher fatigue strength found for VHCF tests at 850 °C in comparison with that at 750 °C and RT, Fig. 3, the distinguishable dislocation features (Fig. 10f and 11b) suggest that the formation of dislocation networks at interface of γ/γ′ might help to prevent further irreversible strain accumulation and in turn delaying the fatigue crack initiation under 850 °C VHCF regime. The dislocation structure and distribution shown in the present work differ markedly from those observed under VHCF loading at 593 °C[57] and 650 °C[8] on Rene 88 DT Ni-base superalloy.

4. Discussion

4.1 Frequency effect

Although the fatigue life data overlapped between 20 kHz and 100 Hz for both RT and 750 °C, Fig. 4, one may still ponder whether the very-high frequency of 20 kHz would cause any changes in the underlying mechanisms that control fatigue deformation and failure. In fact, a similar question was raised by Morrissey and

Golden[14]. When their fatigue data between 20 kHz and 60 Hz were compared, no final conclusion can be made about the frequency effect. One of the possible ways to address this question is to examine the detailed dislocation structure and failure mode. Fig. 12a shows the dislocation structures of the specimen tested at σ_a=350 MPa and 750 °C at 100 Hz, and indeed the presence of dislocation tangles and loops surrounding γ′-precipitates at 100 Hz fatigue test is similar to that at 20 kHz ultrasonic fatigue, as shown in Fig. 10e.

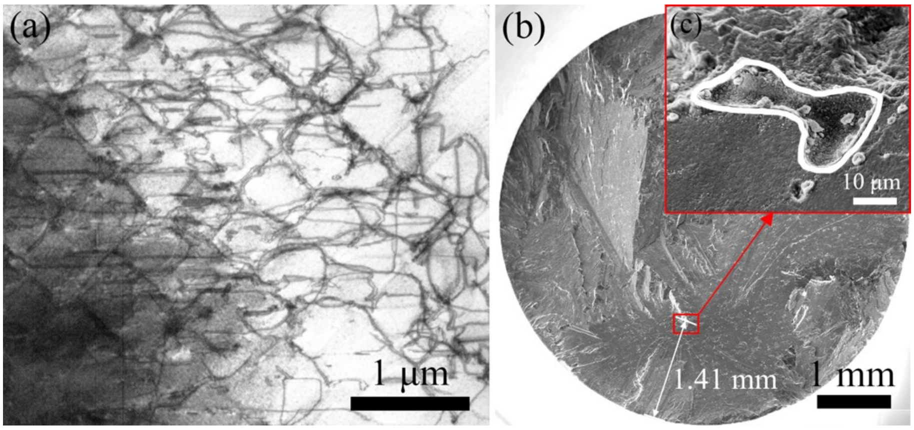

Fig. 12: Fatigue deformation and fracture behavior found on post-fatigued specimen tested at σ_a=350 MPa and 750 °C at 100 Hz, N_f=1.20×10^6: (a) TEM observation showing dislocation structure and distribution; (b) SEM fracture surface showing the crack initiation from the casting pore as outlined in the inset (c).

SEM fractographic observation was made on post-fatigued specimen tested at 100 Hz. Fatigue crack initiation from the internal casting pore located at a distance of 1410 μm to the surface can be seen in Fig. 12b and 12c. It was also confirmed that the fatigue crack grew initially on a large crystallographic plane inclined about 52° with respect to the loading axis (i.e. along {111} octahedral slip planes), followed by the crack deflection to Mode I path perpendicular to the loading axis. Therefore, the failure mode of 100 Hz fatigue is similar to that of 20 kHz as shown in Fig. 5.

Considering the good consistency of the overall fatigue life, deformation mechanism and failure mode between the 20 kHz and 100 Hz, it is reasonable to comment that the ultrasonic fatigue specimen design and test set up (Fig. 2) are well suited to generate the fatigue data at 20 kHz at both RT and 750 °C. Therefore, the crack initiation and early-stage growth behavior as revealed in the present work are most likely to reveal the nature of VHCF fatigue (i.e. no frequency effect in the test conditions studied). No parallel fatigue test was performed at 850 °C with 100 Hz fatigue machine to clarify the frequency effect. But since both the RT and 750 °C fatigue tests showed no frequency effect, it is very unlikely that the fatigue behavior at 850 °C would show a strong frequency dependence.

In the field of VHCF, the mechanism of loading frequency effect on fatigue life is often linked to the specimen self-heating and material's strain-rate sensitivity. As shown in Fig. 3, three RT tests were performed at 350 MPa by intermittent loading, whereas one test by continuous loading. The three intermittently loaded specimens had the fatigue life of 9.17×10^6, 1.09×10^7, and 2.40×10^7 cycles, respectively. These fatigue lives are close to that of 2.10×10^7 obtained with the continuous loading, Fig. 3. In addition, no measurable effect of the loading mode (continuous versus intermittent) on the fatigue life can be found for the tests at 750 °C, Fig. 3. This further substantiates that the frequency effect is insignificant for the VHCF behavior of DZ125 Ni-base superalloy.

4.2 Grain boundary effect

The columnar grain width in the present directionally-solidified Ni-base superalloy was measured as 883.3±40.5 μm (Fig. 1). The area size of Stage I crystallographic cracking region is similar to the measured grain size; this applies to all the representative SEM fractography as shown in Fig. 5. Furthermore, the detailed fractography examination confirmed that both the crack initiation and early-stage growth occurred on a relatively flat crystallographic plane (i.e. no distinct facets of the grain), Fig. 6 and Fig. 8. Thus, the effect of grain boundary on VHCF crack initiation and early-stage crack growth is limited. Cervellon et al.[23] studied the VHCF behavior on both single-crystal and directionally-solidified Ni-base superalloys. When considering the crack initiation and propagation at high temperature, they mentioned that only one specimen showed that the grain boundary had an effect on the crack propagation. For this particular specimen, the fatigue crack was initiated from the surface oxide layers, instead of interior casting pore.[23]

By using compact-tension specimens, Stage I crack propagation rate on a single-crystal NKH-304 under RT fatigue loading was measured as between 8.11×10^{-9} and 2.09×10^{-7} m/cycle[37], while that on a single-crystal CMSX-2 at 700 °C was measured as 1×10^{-8} m/cycle for the shortest crack length[38]. Therefore, the early-stage crack growth rate of the directionally-solidified DZ125 alloy, ranging from 1.61×10^{-9} to 4.38×10^{-8} m/cycle in Table 5, is consistent with the previous work on the single-crystal Ni-base superalloys. Collectively, all the evidence points to that the columnar grain boundary does not affect the VHCF crack initiation and early-stage crack growth behavior at RT and high temperatures.

4.3 Temperature dependence of fatigue strength

The enhanced fatigue strength at 850 °C compared to that at 750 °C and RT in the VHCF regime, Fig. 3, can be attributed to the different temperature dependence of γ′-precipitates and γ-matrix. The strength of γ′-precipitates increased with increasing temperature until reaching the peak strength and then decreased. By comparison, the strength of γ-matrix decreased with increasing temperature. This indicates that the overall strength of γ′-precipitation strengthened DZ125 alloy (60.0% γ′-volume fraction, Fig. 1a) would be determined by the combined effect of γ and γ′-phase.

Feller-Kniepmeier et al.[58] calculated the resolved shear stresses at various temperatures for the respective γ-matrix and γ′-precipitates as well as the overall strength of SRR99 superalloy. The critical resolved shear stress for γ-matrix exhibited a monotonic decrease with increasing temperature, however there was a peak value for γ′-precipitates at 760 °C. Ultimately, this led to the occurrence of peak value of critical resolved shear stress at 550 °C, indicating a combined effect of γ and γ′-phase. Hence, one should not expect the monotonic decrease of material strength with increasing temperature for the present DZ125 alloy. Liu et al.[59] studied the temperature dependence (700, 760, 850 and 900 °C) of high-cycle fatigue on SRR99 superalloy. The fatigue strength was found to increase with increasing temperature initially, reach the peak value at 760 °C and then decrease. They attributed the temperature dependence of the fatigue strength to the strength of γ′-precipitates. In fact, for the above-mentioned reason, we designed the present high-temperature VHCF tests at 750 °C and 850 °C for DZ125 superalloy.

The temperature dependence (20, 550, 760, 850 and 980 °C) of deformation mechanism under monotonic loading on SRR99 superalloy has been discussed in Reference[58]. At relatively low temperature regime, dislocation loops expanded from the γ′-precipitates leading to increased dislocation density in γ-channels. At high temperature regime, dislocations accumulated homogeneously in γ-channels by multiple slip leading to the development of interfacial dislocation networks. For the present DZ125 alloy, the presence of dislocation tangles particularly at γ-channels, Fig. 10e and 11a, can be found for the 750 °C post-fatigued condition, whereas well-developed dislocation networks were observed at the interface of γ/γ′ at 850 °C, Fig. 10f and 11b. Therefore, the distinct dislocation structures between the 750 °C and 850 °C VHCF fatigued DZ125 alloy are analogous to those observed at relatively low and high temperatures for the SRR99 alloy.

At 850 °C, dislocation networks residing in the γ-channels would retard the partial dislocations entering into γ′-precipitates. It was reported in Reference[59] that dislocation networks developed during high-cycle fatigue of SRR99 at high temperature are relatively stable and can accommodate certain amount of cyclic deformation. It is thus reasonable to postulate that the formation of dislocation networks at interface of γ/γ′, Fig. 10f and 11b, help to prevent further irreversible strain accumulation and in turn delaying the fatigue crack initiation of DZ125 alloy under 850 °C VHCF regime. In fact, Feller-Kniepmeier et al.[58] also commented that the build up of γ/γ′ interfacial dislocation networks contributes to material hardening under monotonic loading at high temperature. In sum, the improved fatigue strength at 850 °C under VHCF regime compared with the other two temperatures as shown in Fig. 3 is consistent with the dislocation structures as shown in Fig. 10 and 11.

After clarifying the different temperature dependence of the γ and γ′-phase, we can now rationalize these temperature-dependent fatigue strength as shown in Fig. 3 by correlating with the threshold for propagating the early-stage crack as shown in Fig. 9. In terms of the early-stage crack growth rate as shown in Fig. 9, the threshold of ΔK at 850 °C appears to be higher than that at 750 °C. This means that a higher driving force would be required to trigger the initial crack propagation at 850 °C. In fact, the distance of the first registered beach mark to crack initiation site (i.e. the initial crack length with a measurable crack extension under fatigue load) for 750 °C tests (86 and 127 μm) are much shorter than that for 850 °C tests (533 and 700 μm), Table 4. This also suggests that the crack propagation capability at 750 °C can be activated readily. In other words, the energy needed for propagating a crack at 750 °C is likely to be less when compared to 850 °C. Therefore, the temperature dependence of fatigue strength is consistent with the threshold for early-stage fatigue crack growth.

4.4 Fatigue beach mark creation and early-stage crack growth behavior

The use of intermittent loading mode in VHCF community is a common practice, but the quantitative measurement of early-stage crack growth rate based on beach marks has not been reported yet. Two possible reasons are given here: (i) the applied intermittent loading conditions in previous work did not create regularly spaced beach marks from which the early-stage crack growth rate can be derived; (ii) the early-stage crack growth was often overlooked as the crack initiation took a significant portion of the life. Some VHCF studies reported the presence of beach marks[31–33], but others[43–45,60] did not report their presence at all although showing detailed SEM fractography.

Adams et al.[31] studied the crack initiation and growth on WE43 magnesium under the VHCF intermittent loading. The applied pause times included those of <1 min and >15 min defined as short and long ones, respectively. No pulse/pause conditions were specified when the characteristic beach marks were presented. They commented that beach marks might aid in determining the crack growth rates, but no measurement was performed. Shi et al.[32] studied the VHCF behavior in binary Ti-Al alloys at RT and a pulse/pause time of 0.2/1.8 s was applied. Again, no measurement of crack growth rate was made based on beach marks. The VHCF behavior of Ti6246 alloy at RT in both air and high vacuum and at 300 °C in air was studied by Petit et al.[33] A fixed pulse time of 100 ms was applied, but the pause time varied from 300 ms to 1 s for RT in air, from 300 ms to 800 ms for 300 °C in air, and from 3.5 s to 9.5 s for RT in high-vacuum. Beach marks were found for the RT test in air at σ_a=750 MPa, but no crack growth rate measurement was performed.

Compared to those intermittent loading conditions[31–33], a much shorter pause time was employed in the present work, leading to an overall reduced experimental time. All of the four reported pulse/pause conditions (500/500, 200/200, 120/840, 120/720 ms in Table 4) can create regularly spaced beach marks from which the early-stage crack growth behavior was quantitatively described and cycle-by-cycle crack growth rate are presented in Fig. 9. Since the growth rate was measured based on the distance between two adjacent beach-mark division boundaries, this implies that the creation of beach marks is a consequence of load pause.

The observed division boundary was very similar in thickness and roughness for all of the registered beach marks, Fig. 7a, 8c and 8d. This is with our expectation as a constant pulse/pause time was used per test specimen. The fine beach-mark division boundaries are probably due to the relatively short pause time employed. When the prolonged pause time (>15 min) was used to create beach marks in WE43 magnesium, the division boundaries tended to be much enhanced in their thickness and roughness. However, much finer division boundaries were found for the shorter pause times (<1 min). This seems to highlight the importance of using the optimized pause condition (i.e. as short as possible) to create visible but fine beach marks. As a result, the measured crack growth rate should be least affected by the beach-mark creation method.

For all four specimens, it does not seem that the pulse/pause conditions caused any abnormal early-stage crack growth behavior at 750 and 850 °C, Fig. 9. However, since these tests only covered a limited value range of σ_a, it is not appropriate to draw a conclusion here. As pointed out by Shi et al.[32], the presence of beach marks might be related to the level of ΔK as they were commonly found within the crack propagation region with a relatively low ΔK value of less than 3 MPa $m^{1/2}$. Our future work will focus on clarifying the formation mechanism of the beach marks by the VHCF intermittent loading mode.

With the use of optimized intermittent loading conditions, both the initiation and early-stage crack growth processes in VHCF regime at high temperatures were successfully tracked. The first registered beach mark can be as close as only 86 μm distance to the crack initiation site, Table 4. It can be seen in Fig. 7a, 8c and 8d that the distance between adjacent beach marks increased with the increasing crack length over the whole early-stage crack growth process. This means that crack growth behavior that occurs on the crystallographic plane is a steady process, i.e. the crack propagation within the Stage I cracking region follows the classic Paris law as shown in Fig. 9. This finding is intriguing as it is closely related to the accuracy of predicting the remaining life to failure by using a fracture mechanics approach to study the propagation of cracks. This holds the promise to perform a damage tolerance design of engineering structures against VHCF.

Caton and Jha[61] compared the small and long fatigue crack growth behaviors at 650 °C on IN 100 polycrystalline Ni-base superalloy. The small crack growth rate was monitored using replication technique. The small crack growth rate was measured as 1×10^{-9} and 1×10^{-8} m/cycle for a crack length of 93 and 128 μm. Hence the presently measured early-stage crack growth rate, Table 5, is consistent with the previous high-temperature fatigue work[61]. In addition, the growth rate for long cracks was measured as between 5×10^{-8} and 5×10^{-6} m/cycle for crack length of 200 to 7200 μm. For the determination of long fatigue crack growth rate, a compact tension specimen was used.[61] Recall that the maximum crack length for the Stage I cracking was 2690 μm and the corresponding crack growth rate was measured as 4.38×10^{-8} m/cycle (Table 5). Therefore, the crack growth rate in Stage I cracking region at later stage agrees well with the lower bound value of the long crack as reported in Reference[61].

Based on the applied pulse/pause time as well as the first and last registered beach mark locations, the number of cycles spent for propagating the crack within Stage I cracking region can be derived. At 750 °C, the life consumed was calculated as 2.30×10^5 for σ_a=300 MPa and 1.28×10^5 for σ_a=275 MPa, while 3.84×10^4 for σ_a=350 MPa and 2.06×10^4 for σ_a=300 MPa at 850 °C. This implies that at the higher temperature, crack requires less fatigue cycles to trigger the final specimen failure once the crack propagation capability is activated. By contrast, the early-stage crack growth rate is not largely affected by the applied stress, Table 5. In addition, the fraction of fatigue life spent for the early-stage crack growth becomes smaller with decreasing stress level, Table 5. In this context, the present observation is consistent with the consensus that under VHCF regime, the cycles spent for interior crack initiation can consume a very large fraction of the fatigue life (i.e. N_i/N_f of between 90% and 99%[6,20]).

4.5 VHCF fatigue life prediction

All of the fractured specimens (Fig. 3) showed exclusively the interior fatigue cracking and majority of the specimens revealed that crack initiation from the casting pore. Fig. 13a provides the collection of measured casting pore data (750 °C) on a graph of ΔK_{pore} versus N_f by combining their sizes as well as the site distance to surface. It can be found in Fig. 13a that the fatal casting pore as the interior fatigue cracking origin is not necessarily the largest one, neither the closet one to the surface, indicating of a combined effect. As a result, an attempt was made to correlate the stress intensity factor amplitude calculated around the pore (ΔK_{pore}) with the cycles to failure.

The stress intensity factor amplitude around the casting pore, ΔK_{pore}, can be calculated following equation proposed by Murakami et al.[50]:

$$\Delta K_{\mathrm{pore}} = 0.5\sigma_{\mathrm{a}}\sqrt{\pi\sqrt{area_{\mathrm{pore}}}} \tag{7}$$

where the shape factor is taken as 0.5 for the case of internal crack initiation as opposed to a value of 0.65 that was used for the near-to-surface one [50]. Instead of using the equivalent area of the pore, the equation was adapted slightly in the present work, as given below:

$$\Delta K_{\mathrm{pore}} = 0.5\sigma_{\mathrm{a}}\sqrt{\pi b} \tag{8}$$

where b is defined as the initial defect size that was measured on the basis of the half-length along the major axis of the casting pore (as shown schematically in Fig. 6a).

An inverse relationship can be found for 750 °C VHCF data between ΔK_{pore} and N_f, Fig. 13a. The ΔK_{pore} calculation equation is also added onto the figure to show that this term indeed considered the contribution of both the applied far-field stress and the initial pore size as crack initiation site. For the other two temperatures (RT and 850 °C), the number of tests is not sufficient to allow us to draw a conclusion, Fig. 13b.

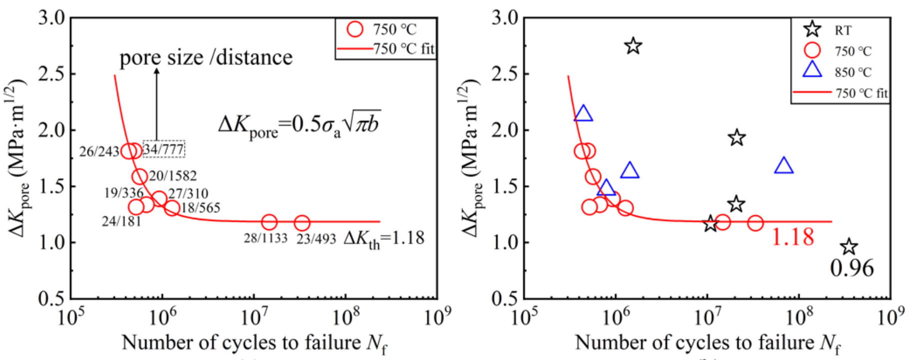

(a) (b)

Fig. 13: (a) A collection of measured casting pore data in terms of their sizes and the site distance to surface on a graph of ΔK_{pore} versus N_f for 750 °C tests; (b) Calculated

stress intensity factor amplitude around the casting pore, ΔK_{pore}, against the cycles to failure, N_f for all three temperatures of RT, 750, 850 °C. Determinations of the threshold of ΔK are also denoted in the figure.

Steuer et al.[12] considered the fatigue crack initiation size dependence of AM1 single-crystal Ni-base superalloy by using the fatigue indicator parameter (FIP) approach in the form given in Eq. 9. Similarly, using the FIP approach, Castelluccio and McDowell[62] described small fatigue crack initiation and growth on single-crystal copper under high-cycle fatigue regime. Therefore, it is interesting to examine whether the FIP approach can be used for the present VHCF data obtained on DZ125 alloy. The calculation of FIP was according to[12]:

$$\mathrm{FIP} = \frac{\mu\sigma_a}{E_d}\left[1 + k\frac{\Delta K_{pore}}{\Delta K_{th}}\right] \tag{9}$$

where μ is the Schmid factor, E_d is the dynamic elastic modulus, k is a constant. A value of μ=0.408 is used as this represents the octahedral slip with applied stress along the [001] direction.[23] k=1 was chosen, that is consistent with that used for single-crystal AM1 alloy fatigue study[12], and E_d=103 GPa (as given for 750 °C test temperature in Table 3). ΔK_{pore} is the stress intensity factor amplitude as defined in Eq. 8 and this is normalized with respect to the threshold of ΔK_{th} for early-stage crack propagation. The magnitude of ΔK_{th}=1.18 MPa m$^{1/2}$ for the VHCF tests at 750°C was determined from Fig. 13 when the ΔK_{pore}-N_f curve appears to become flat and to asymptotically approach the minimum value. In addition, for the VHCF tests at RT, ΔK_{th}=0.96 MPa was simply determined by the use of the minimum value of ΔK_{pore} because of the very limited number of tests performed.

The determined FIP values for both RT and 750 °C are presented in Fig. 14a. It is not possible to report the FIP results at 850 °C as there were only 8 tests performed at this temperature, Fig. 3, and it was difficult to determine ΔK_{th} for this temperature, Fig. 13b. Within this specimen group, 4 out of 6 failed specimens showed the presence of casting pores as the crack initiation site. It can be seen in Fig. 14a that the fatigue lives increased with the decreasing value of FIP. The data fitting equations for connecting N_f and FIP are given for both RT and 750 °C. It is worth pointing out that fatigue results from different temperature conditions were indirectly normalized as the FIP calculation was based on the temperature dependent E_d in Eq.

9. However, this does not create the opportunity to obtain one empirical power law from all the results in Fig. 14a. In other words, no single trend line with all data lay on can be found. This may suggest the limitation of the FIP approach. The comparison of the FIP model predicted fatigue life with experimental data at RT and 750 °C is shown in Fig. 14b. The model predictions are within a factor of three of experimental results, indicating a reasonably good agreement, but with an exception of two data point for 750 °C. Since the FIP approach used here does not consider the contribution of early-stage crack growth process, the results indicate that fatigue crack initiation is an important factor affecting the fatigue life in the regime of VHCF and high-cycle fatigue.

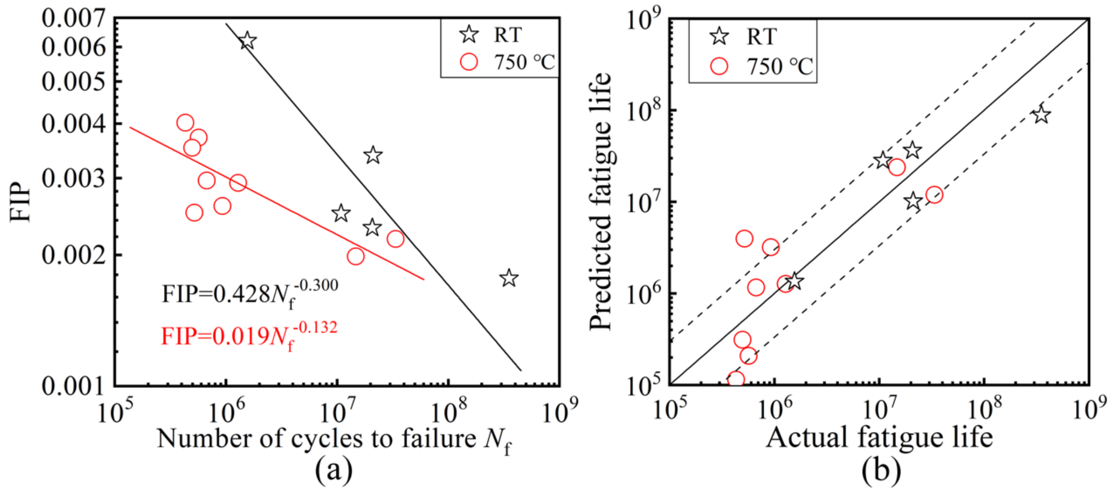

Fig. 14: (a) Determined relationship between the FIP values and fatigue lives; (b) Model predicted fatigue lives in comparison with the experimental data.

Since there was an angle of approx. 52° between the initial cracking plane and the far-field loading axis for stage I cracking (Fig. 5), one might question whether the use of ΔK considering Mode I crack is appropriate for the present crystallographic Stage I cracking. It was reported by Socie and Shield[63] that a tensile mean stress across the crack plane would tend to hold it open, assist in its growth and have an effect similar to the normal strain. Thus, it is postulated that the resolved normal stress on this crystallographic plane assists in the early-stage crack propagation. This also implies that there will be no difference between the use of far-field stress and resolved normal stress in terms of the calculated FIP results. This is with our expectation as the presence of $\Delta K_{pore}/\Delta K_{th}$ in Eq. 9 means that the conversion factor of sin 52° for resolved normal stress calculation would be cancelled by itself when applying $\Delta K_{pore}/\Delta K_{th}$.

In terms of the FIP calculation, the present FIP model and the other FIP models (e.g. that adopted in Reference[12]) were all developed based on the one originally proposed by Fetami and Socie[64]. The original FIP model based on critical plane approach that primarily considered the contribution of fatigue crack initiation. This means that the FIP approach assumed that fatigue crack initiation involves localized plastic deformation in persistent slip bands even in the high-cycle fatigue region. However, the fatigue life of a defect-containing body cannot be predicted using the original stress-based FIP model. To overcome this problem, Steuer et al.[12] proposed a modified FIP model by taking into account the casting pore size through ΔK to predict the relationship between FIP and low-cycle fatigue lifetime. In fact, a similar FIP approach has been adopted by Cervellon et al.[23,48] to study the VHCF lifetime on CMSX-4, AM1, MCNG and DS200 Ni-base superalloys, and by Ormastroni et al.[65] to study low-cycle fatigue, high-cycle fatigue and VHCF lives on a third-generation single-crystal Ni-base superalloy. The primary difference between the present FIP approach and the previous ones in References[23,48,65] is that the half-length along the major axis of the casting pore, b, was used to derive the ΔK_{pore} in Eq. 8. Both the equivalent area of the pore and its half-length along the minor axis were attempted. It proved that the data relationship between the calculated FIP values based on b and N_f can be reasonably well fitted by a single straight line.

Murakami et al. [50] derived a conversion factor between the square root of defect area in the case of surface cracking and that in the case of interior cracking (i.e. near-to-surface or interior defect) under the condition that the same value of stress intensity factor can be admitted. The fatigue strength σ_w prediction equation proposed by Murakami [50] is given below:

$$\sigma_w = 1.56(\mathrm{HV}+120)/(\sqrt{\mathrm{area}})^{1/6} \tag{10}$$

where HV is the Vickers hardness and $\sqrt{\mathrm{area}}$ indicates the square root of the area of a defect that appears not to be at the surface. Based on this model, Wang et al. [17] made a small adjustment by incorporating the fatigue lives N_f, as following.

$$\sigma_w = (3.09-0.12\lg N_f)(\mathrm{HV}+120)/(\sqrt{\mathrm{area}})^{1/6} \tag{11}$$

For our specific case, this fatigue strength equation has been further adapted by using the value of half-length along the major axis of the casting pore, b, instead of $\sqrt{\text{area}}$ as given in Eq. 12. This led to the equation as follows:

$$\sigma_{\mathrm{w}} = (\alpha - \beta \lg N_{\mathrm{f}})(\mathrm{HV} + 120) / b^{1/6} \qquad (12)$$

where materials constants α and β are the best fit values in terms of the minimized squared residuals while performing regression analysis. The values of Vickers hardness (HV) for RT, 750 °C and 850 °C are given in Table 3. Fig. 15 shows the comparison between the predicted fatigue strengths and experimental ones. It is evident that the model predictions based on b (Eq. 12) are within a factor of 1.2 of experimental results. In addition, model predictions based on $\sqrt{\text{area}}$ of the casting pore seems to create less accuracy compared to those based on its half-length along the major axis, Fig. 15.

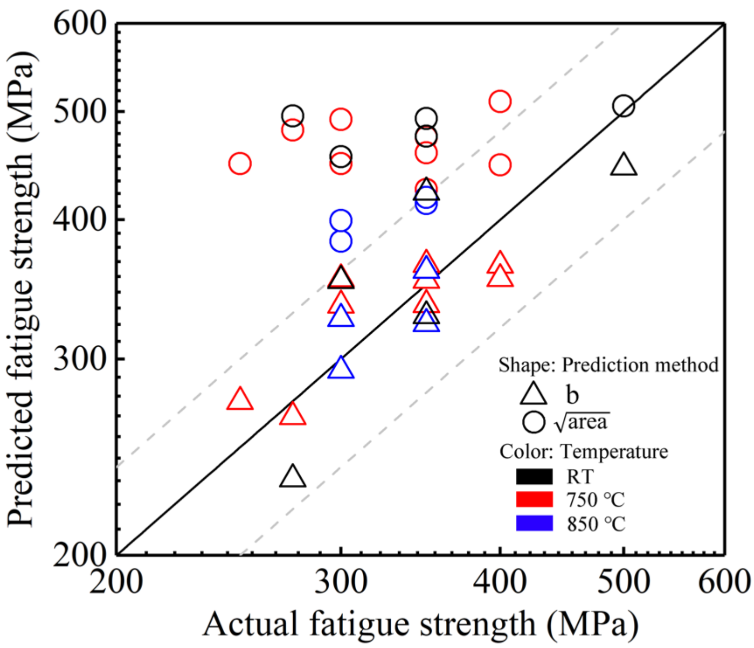

Fig. 15: Comparison of predicted fatigue strengths with experimental obtained ones that cover all three temperatures.

5. Conclusions

Crack initiation and early-stage growth of a directionally-solidified Ni-base superalloy DZ125 under VHCF regime at high temperatures were studied. Most fatigue cracks initiated from a single and internal casting pore, followed by early-stage crack growth on large {111} crystallographic plane (i.e. Stage I cracking) until the crack length is large enough to trigger the Mode I crack propagation (i.e. Stage II cracking). The five key aspects can be summarized:

1) The ultrasonic fatigue testing at 20 kHz does not seem to cause noticeable changes in fatigue life, deformation mode as well as fracture mechanism, when compared to that at 100 Hz.
2) The fatigue strength at 850 °C is higher than that at 750 °C and RT in the VHCF regime, i.e. at low stress regime. This can be attributed to the different temperature dependence of γ′-precipitates and γ-matrix. At 850 °C, the presence of dislocation networks residing in the γ-channels would retard the partial dislocations entering into γ′-precipitates, accounting for the improved fatigue strength.
3) Creation of fine but visible fatigue beach marks within the Stage I cracking region can be achieved with the optimized intermittent VHCF loading condition. The early-stage crack growth was revealed as a steady process based on the measurement of registered beach marks.
4) The enhanced fatigue strength at 850 °C can be rationalized with the higher threshold for propagating the early-stage crack.
5) FIP based fatigue life and strength predictions were performed and compared with experimental data. The model calculation based on the half-length along the major axis of the casting pore is most suited for the present case.

Acknowledgement

Zihua Zhao acknowledges financial supports by the National Natural Science Foundation of China (91860110) and the National Science and Technology Major Project of China (2017-IV-0012-0049). Bo Chen acknowledges financial supports by the UK's Engineering and Physical Sciences Research Council, EPSRC First Grant Scheme EP/P025978/1 and Early Career Fellowship Scheme EP/R043973/1. In addition, Bo Chen extends his sincere thank you to Prof. Sheng-kai Gong at Beihang University to provide additional financial support.

References

1 B.A. Cowles: *Int. J. Fract.*, 1996, vol. 80, pp. 147–63.

2 *Engine Structural Integrity Program (ENSIP) MIL-HDBK-1783B*, Department of Defense Handbook.

3 M.D. Chapetti, T. Tagawa, and T. Miyata: *Mater. Sci. Eng. A*, 2003, vol. 356, pp. 236–44.

4 S. Nishijima and K. Kanazawa: *Fatigue Fract. Engng. Mater. Struct.*, 1999, vol. 22, pp. 601–7.

5 W. Li, H. Yuan, Z. Sun, and Z. Zhang: *Int. J. Fatigue*, 2014, vol. 64, pp. 42–53.

6 Z. Huang, D. Wagner, C. Bathias, and P.C. Paris: *Acta Mater.*, 2010, vol. 58, pp. 6046–54.

7 Q.Y. Wang, C. Bathias, N. Kawagoishi, and Q. Chen: *Int. J. Fatigue*, 2002, vol. 24, pp. 1269–74.

8 J.C. Stinville, E. Martin, M. Karadge, S. Ismonov, M. Soare, T. Hanlon, S. Sundaram, M.L.P. Echlin, P.G. Callahan, W.C. Lenthe, J. Miao, A.E. Wessman, R. Finlay, A. Loghin, J. Marte, and T.M. Pollock: *Metall. Mater. Trans. A*, 2018, vol. 49, pp. 3865–73.

9 D. Texier, J. Cormier, P. Villechaise, J.C. Stinville, C.J. Torbet, S. Pierret, and T.M. Pollock: *Mater. Sci. Eng. A*, 2016, vol. 678, pp. 122–36.

10 M.L. Zhu, L. Jin, and F.Z. Xuan: *Acta Mater.*, 2018, vol. 157, pp. 259–75.

11 Y. Murakami, T. Nomoto, and T. Ueda: *Fatigue Fract. Engng. Mater. Struct.*, 1999, vol. 22, pp. 581–90.

12 S. Steuer, P. Villechaise, T.M. Pollock, and J. Cormier: *Mater. Sci. Eng. A*, 2015, vol. 645, pp. 109–15.

13 M. Lamm and R.F. Singer: *Metall. Mater. Trans. A*, 2007, vol. 38, pp. 1177–83.

14 R.J. Morrissey and P.J. Golden: *Int. J. Fatigue*, 2007, vol. 29, pp. 2079–84.

15 S. Heinz and D. Eifler: *Int. J. Fatigue*, 2016, vol. 93, pp. 301–8.

16 O. Umezawa and K. Nagai: *Metall. Mater. Trans. A*, 1998, pp. 809–22.

17 Q.Y. Wang, J.Y. Berard, A. Dubarre, G. Baudry, S. Rathery, and C. Bathias: *Fatigue Fract. Engng. Mater. Struct.*, 1999, vol. 22, pp. 667–672.

18 Y. Hong, Z. Lei, C. Sun, and A. Zhao: *Int. J. Fatigue*, 2014, vol. 58, pp. 144–51.

19 K. Shiozawa, Y. Morii, S. Nishino, and L. Lu: *Int. J. Fatigue*, 2006, vol. 28, pp. 1521–32.

20 N. Ranc, D. Wagner, and P.C. Paris: *Acta Mater.*, 2008, vol. 56, pp. 4012–21.

21 E. Bayraktar, I.M. Garcias, and C. Bathias: *Int. J. Fatigue*, 2006, vol. 28, pp. 1590–602.

22 J.Z. Yi, C.J. Torbet, Q. Feng, T.M. Pollock, and J.W. Jones: *Mater. Sci. Eng. A*, 2007, vol. 443, pp. 142–9.

23 A. Cervellon, J. Cormier, F. Mauget, Z. Hervier, and Y. Nadot: *Metall. Mater. Trans. A*, 2018, vol. 49, pp. 3938–50.

24 J. Miao, T.M. Pollock, and J. Wayne Jones: *Acta Mater.*, 2009, vol. 57, pp. 5964–74.

25 J.C. Stinville, W.C. Lenthe, J. Miao, and T.M. Pollock: *Acta Mater.*, 2016, vol. 103, pp. 461–73.

26 D. Eylon and C.M. Pierce: *Metall. Trans. A*, 1976, vol. 7, pp. 111–21.

27 M. Zimmermann: *Int. Mater. Rev.*, 2012, vol. 57, pp. 73–91.

28 S. Stanzl-Tschegg: *Int. J. Fatigue*, 2014, vol. 60, pp. 2–17.

29 K. Tanaka and Y. Akiniwa: *Fatigue Fract. Engng. Mater. Struct.*, 2002, vol. 25, pp. 775–84.

30 C. Sun, Q. Song, Y. Hu, and Y. Wei: *Int. J. Fatigue*, 2018, vol. 117, pp. 9–12.

31 J.F. Adams, J.E. Allison, and J.W. Jones: *Int. J. Fatigue*, 2016, vol. 93, pp. 372–86.

32 Q. Shi, S.A. Hsie, J.W. Jones, and J.E. Allison: *Mater. Sci. Eng. A*, 2019, vol. 756, pp. 564–77.

33 J. Petit, C. Sarrazin-Baudoux, J. Martinez, S. Stanzl-Tschegg, and H. Mayer: in *4th International Conference on Very High Cycle Fatigue (VHCF-4)*, TMS (The Minerals, Metals & Materials Society), 2007, pp. 399–408.

34 Y. Li, X. Zhang, D. Parfitt, S. Jones, and B. Chen: *Mater. Charact.*, 2019, vol. 151, pp. 542–52.

35 D.J. Duquette, M. Gell, and J.W. Piteo: *Metall. Trans.*, 1970, vol. 1, pp. 3107–15.

36 M. Gell, G.R. Leverant, and J.W. Piteo: *Acta Metall.*, 1968, vol. 16, pp. 553–61.

37 M. Sakaguchi, R. Komamura, X. Chen, M. Higaki, and H. Inoue: *Int. J. Fatigue*, 2019, vol. 123, pp. 10–21.

38 B.F. Antolovich, A. Saxena, and S.D. Antolovich: *J. Mater. Eng. Perform.*, 1993, vol. 2, pp. 489–96.

39 H. Peng, Y. Shi, S. Gong, H. Guo, and B. Chen: *Mater. Des.*, 2018, vol. 159, pp. 155–69.

40 C. Bathias and P.C. Paris: *Gigacycle Fatigue in Mechanical Practice*, Marcel Dekker, New York, 2005.

41 Y. Furuya: *Mater. Lett.*, 2013, vol. 112, pp. 139–41.

42 C. Ragazzo, R.. Hertzberg, and R. Jaccard: *J. Test. Eval.*, 1995, vol. 23, pp. 19–26.

43 H. Ishii, T. Yagasaki, and H. Akagi: *Fatigue Fract. Eng. Mater. Struct.*, 2002, vol. 25, pp. 831–5.

44 S. Stanzl-Tschegg and B. Schönbauer: *Procedia Eng.*, 2010, vol. 2, pp. 1547–55.

45 U. Karr, R. Schuller, M. Fitzka, A. Denk, A. Strauss, and H. Mayer: *Mater. Test.*, 2017, vol. 59, pp. 438–44.

46 *HB 5287-96: Fatigue Test Method of Metal Loaded Along Axial Direction*, Aviation Industry Corporation of China.

47 N. Kawagoishi, Q. Chen, and H. Nisitani: *Fatigue Fract. Eng. Mater. Struct.*, 2000, vol. 23, pp. 209–16.

48 A. Cervellon, J. Cormier, F. Mauget, and Z. Hervier: *Int. J. Fatigue*, 2017, vol. 104, pp. 251–62.

49 Y. Murakami and M. Endo: *Fatigue*, 1994, vol. 16, pp. 163–82.

50 Y. Murakami, S. Kodama, and S. Konuma: *Int. J. Fatigue*, 1989, vol. 11, pp. 291–8.

51 I. Marines-Garcia, P.C. Paris, H. Tada, C. Bathias, and D. Lados: *Eng. Fract. Mech.*, 2008, vol. 75, pp. 1657–65.

52 M. Geuffrard: PhD Thesis, Ecole des Mines ParisTech, Paris, 2010.

53 S. Kraft, R. Zauter, and H. Mughrabi: *Fatigue Fract. Engng. Mater. Struct.*, 1993, vol. 16, pp. 237–53.

54 C. Stöcker, M. Zimmermann, and H.J. Christ: *Int. J. Fatigue*, 2011, vol. 33, pp. 2–9.

55 S. Nategh and S.A. Sajjadi: *Mater. Sci. Eng. A*, 2003, vol. 339, pp. 103–8.

56 A.K. Singh, N. Louat, and K. Sadananda: *Metall. Trans. A*, 1988, vol. 19, pp. 2965–73.

57 J. Miao, T.M. Pollock, and J. Wayne Jones: *Acta Mater.*, 2012, vol. 60, pp. 2840–54.

58 M. Feller-Kniepmeier, T. Link, I. Poschmann, G. Scheunemann-Frerker, and C. Schulze: *Acta Mater.*, 1996, vol. 44, pp. 2397–407.

59 Y. Liu, J.J. Yu, Y. Xu, X.F. Sun, H.R. Guan, and Z.Q. Hu: *Mater. Sci. Eng. A*, 2007, vol. 454–455, pp. 357–66.

60 C. Sun, Q. Song, L. Zhou, J. Liu, Y. Wang, X. Wu, and Y. Wei: *Int. J. Fatigue*, 2019, vol. 124, pp. 483–92.

61 M.J. Caton and S.K. Jha: *Int. J. Fatigue*, 2010, vol. 32, pp. 1461–72.

62 G.M. Castelluccio and D.L. McDowell: *Int. J. Fract.*, 2012, vol. 176, pp. 49–64.

63 D.F. Socie and T.W. Shield: *J. Eng. Mater. Technol.*, 1984, vol. 106, pp. 227–32.

64 A. Fatemi and D.F. Socie: *Fatigue Fract. Eng. Mater. Struct.*, 1988, vol. 11, pp. 149–65.

65 L.M.B. Ormastroni, L.M. Suave, A. Cervellon, P. Villechaise, and J. Cormier: *Int. J. Fatigue*, 2020, vol. 130, p. 105247.